NASA TECHNICAL TRANSLATION NASA TT F-14447

# SATELLITE METEOROLOGY

## Table of Contents, Figure and Table Titles

K.S. Shifrin and V.L. Gayevskiy, eds.

(NASA-TT-F-14447) SATELLITE METEOROLOGY Table of Contents, Figure and Table Titles K.S. Shifrin, et al (NASA) Jun. 1972 14 p CSCL 04B

N73-10616

Unclas
G3/20 46265

Translation of Table of Contents, Figure and Table Titles of Sputnikovaya Meteorologiya, Edited by K.S. Shifrin and V.L. Gayevskiy, Trudy No. 221 of the Main Geophysical Observatory imeni A.I. Voyekov, Leningrad, Hydrometeorological Press, 1968

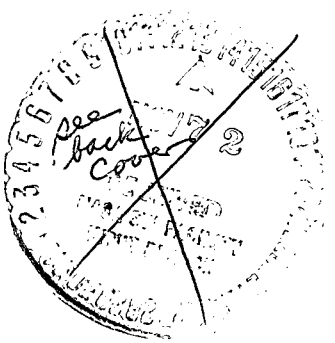


NATIONAL AERONAUTICS AND SPACE ADMINISTRATION
WASHINGTON, D.C. 20546 JUNE 1972

Page

ACTINOMETRIC APPARATUS USED ON SOVIET WEATHER SATELLITES 3

Fig. 1. Optical design of narrow-angle apparatus. 4

Fig. 2. Optical design of wide-angle apparatus. 4

Fig. 3. Scheme for the collection of actinometric information. 5

Fig. 4. Output characteristics of actinometric apparatus. 6

PRINCIPLES OF CALIBRATING LONG-WAVE ACTINOMETRIC APPARATUS USED ON WEATHER SATELLITES 8

Fig. 1. The relationship between the radiation factor of a cavity and the radiation capability of its internal coating. 11

INFORMATION PROPERTIES OF A SCANNING INFRARED APPARATUS USED ON WEATHER SATELLITES 14

STATISTICAL CHARACTERISTICS OF SIGNALS RECEIVED FROM A SCANNING INFRARED APPARATUS 21

Fig. 1. Laws of distribution of video signals from a water surface. I, Pacific Ocean: 64-82°N; 110-107°E; 2 hrs 40 min. $\overline{u} = 42.39$, $\sigma = 5.96$; II, Open section of the Mediterranean Sea: 32-35°N, 29-27°E; 10 hrs 00 min, $\overline{u} = 60.89$, $\sigma = 9.7$. 25

Fig. 2. Laws of distribution of video signals received from a dry land surface. I, Continent (Center of the European Territory of the Soviet Union), 10 hrs 08 min, $\overline{u} = 43.68$, $\sigma = 4.78$; II, Continent (South America); 39-36°S, 68-66°W, 6 hrs 05 min, $\overline{u} = 61.01$, $\sigma = 4.65$. 26

Fig. 3. Laws of distribution of video signals received from a cyclone. I, Cyclone over the West Siberian Lowlands, $\overline{u} = 26.2$, $\sigma = 4.38$; II, Cyclone over the Atlantic Ocean: 48-54°N, 22-14°W, 9 hrs 15 min, $\overline{u} = 33.14$, $\sigma = 10.49$. 26

Fig. 4. Laws of distribution of video signals received from frontal cloudiness. I, Frontal cloudiness over ETC[1]; 10 hrs 6 min - 10 hrs 14 min, $\overline{u} = 23.29$, $\sigma = 8.58$; II, Frontal cloudiness over the Pacific Ocean: 43.5-54°S, 162-176°E, 1 hr, $\overline{u} = 40.31$, $\sigma = 5.76$. 27

Fig. 5. Laws of distribution of video signals received from cyclonic cloudiness, cumuli and from the surface of the ocean. 27

[1]ETC - European Territory of the Soviet Union.

Page

Table 1. Numerical characteristics of the laws of distribution of signal amplitudes of an infrared apparatus over the radiating surfaces being investigated. 28

AUTOMATIC PROCESSING OF INFRARED INFORMATION RECEIVED FROM WEATHER SATELLITES 30

Fig. 1. Data sheet prepared from the results of automatic processing of infrared information received from the Cosmos-122 and Cosmos-144. 33

Fig. 2. Field of radiation temperature based on the results of the observations made by Cosmos-122. 34

Fig. 3. Weather in the observation region of Cosmos-122 at 15 hrs, 2 July 1966. 34

Fig. 4. Structure of cloudiness as calculated on the basis of photography. 35

Table 1. Contrast characteristics within the field of radiation temperature, as based on the results of observations made by Cosmos-122 and Cosmos-144. 36

COMPARISON OF THE RESULTS OF LAND-BASED, AERIAL AND SATELLITE MEASUREMENTS 38

Fig. 1. Course followed by the subsatellite point (3), the aircraft (2), boundary of the information zone of loop number 296 of Cosmos-156, (1). 40

Fig. 2. Distribution of cloudiness over the ETC on 17 May 1967 at 12 hrs 44 min, Moscow standard time, on the basis of data from ground stations: 1, no cloudiness; 2, slight cloudiness; 3, Ci; 4, significant cloudiness at the lower level; 5, dense cloudiness at the lower level. 41

Fig. 3a. Distribution of reflected short-wave radiation on the basis of data from ground stations, 17 May 1967 at 12 hrs 44 min, Moscow standard time. 42

Fig. 3b. Geographical distribution of reflected short-wave radiation on the basis of information received from Cosmos-156 on loop number 296, 17 May 1967. 42

Fig. 4a. Geographical distribution of ground temperature, on the basis of ground information received at 12 hrs 44 min, Moscow standard time, 17 May 1967. 44

Fig. 4b. Geographical distribution of radiation temperature on the basis of measurements made by Cosmos-156 on loop number 296, 17 May 1967. 45

Page

Table 1. Rising long-wave fluxes at the level of the aircraft, for various cloud levels. 47

Table 2. Comparison of the results of measurements made at the subsatellite point $I_o$, cal/cm$^2$-min-sterad, $\pi J_o$, P, Sh, $E_p^{\uparrow}$ in cal/cm$^2$-min 48-49

THE UTILIZATION OF DATA ON THE FIELD OF RISING SHORT-WAVE RADIATION OBTAINED FROM THE COSMOS-122 50

Introduction 50

Data of Measurements Made by the Cosmos-122 50

Fig. 1. Sample of the numerical data on Radiation in the 0.3-3 μm portion of the spectrum, obtained 17 August 1966 from the Cosmos-122. 52

Fig. 2. Cloud map obtained from the Cosmos-122 on 17 August 1966 during the period 5 hrs 44 min - 5 hrs 50 min, Moscow time. 53

Processing and Analysis of Data 53

Fig. 3. Representations of the brightness field at various subsatellite points (Moscow time).
a, Loop No. 501, 29 July 1966; b, Loop No. 560, 28 July 1966;
c, Loop No. 898, 25 July 1966 54

Fig. 4. Realization of the brightness field at various subsatellite points, Moscow time, Loop No. 853, 21 August 1966. 55

Fig. 5. Representation of the brightness field at various subsatellite points, Moscow time, Loop No. 913, 26 August 1966. 55

Fig. 6. Flight trajectory of the Cosmos-122. I, Loop No. 767, 16 August 1966; II, Loop No. 898, 25 August 1966; III, Loop No. 913, 26 August 1966. 56

Angular Structure of the Field of Outgoing Short-Wave Radiation 57

Fig. 7. Indicatrixes of the clarity field of reflected radiation over water. 1, Reyleigh curve; 2, Received from the Tyros-IV; 3, Received from the Cosmos-122. 58

Table 1. Results of Observations made with Cosmos-122 at various subsatellite points 59

29 July 1966, Loop No. 501 59

Page

2 August 1966, Loop No. 560 60

21 August 1966, Loop No. 853 61

Table 2. Results of calculations of the radiation balance of the atmosphere. 62

16 August, Loop No. 767 62

21 August, Loop No. 853 63

25 August, Loop No. 898 63

26 August, Loop No. 913 64

PROBLEMS OF INTERPRETING INFRARED IMAGES OF CLOUDINESS OBTAINED FROM WEATHER SATELLITES 66

1. Estimating the Possible Deviations from the Mean Value of the Contrasts of Radiation Temperatures 67

Table 1. Mean square deviations $\delta$ of cloud- and ground- temperature contrasts by day (line 1) and by night (line 2), for 12 months 68-69

Fig. 1. Probability of the distribution of deviations of contrasts of cloud radiation temperatures against the background of the underlying surface, from mean perennial values in winter (1) and summer (2). a, Cloudiness at lower level; b, Cloudiness at middle level 68

2. The effect of Various Factors on the Magnitude of Contrasts of Radiation Temperatures 69

Table 2. Error $\Delta t$ in magnitude of the contrasts of the radiation temperatures of clouds against the background of the terrestrial surface, as the result of not allowing for the radiation peculiarities of natural surfaces 70

Table 3. The effect of the degree of cloudiness on the magnitude fluxes of outgoing radiation I and contrasts of radiation temperatures $\Delta t$ of cloudiness against the background of the underlying surface (8.0-13.0 $\mu$m) 72

Fig. 2. Relative angular distribution on the intensity of outgoing radiation in transparency windows of the atmosphere, 8.0-13.0 $\mu$m (a) and 3.5-4.0 $\mu$m (b). 1, Leningrad, January; 2, Leningrad, July; 3, Ashkhabad, January; 4, Ashkhabad, July; 5, Yakutsk, January; 6, Kiev, July. 73

Page

Fig. 3. Angular dependence of the contrasts of radiation temperatures of cloudiness at the lower level, against a background of the underlying surface, in transparency windows of the atmosphere, 8.0-13.0 μm (a) and 3.5-4.0 μm (b). The symbols used in this figure are the same as in Figure 2. 74

Table 4. The effect of spectral transmission $\tau_\lambda$ of the barometer filter system on the magnitude of temperatures measured by the radiation method 75

3. Corrections to the Temperature of the Underlying Surface and the Clouds as Measured by the Radiation Method 76

Fig. 4. Probability of the distribution of error for a given temperature of the underlying surface by the radiation method at night with a cloudless sky, in various radiation windows. 1) 3.5-4.0 μm; 2) 8.0-13.0 μm; 3) 4.5-5.0 μm. 76

Fig. 5. Probability of distribution of error in determining the temperature of the upper boundary of the lower level of cloudiness by the radiation method at night. Symbols used are the same as those in Figure 4. 76

Table 5. Corrections Δt to the temperature of the radiating surface, as determined by the radiation method from weather satellites. (the first line is for 3.5-4.0 μm; the second line is for 4.5-5.0 μm; the third line is for 8.0-13.0 μm) 77

4. Analysis of Infrared Images of the Earth Obtained from Weather Satellites 79

Fig. 6a. Infrared image of the underlying surface and of the clouds, obtained from the Nimbus-1 on 15 September 1964 (Loop No. 258, 3 hrs, Moscow time). 80

Fig. 6b. Synoptic situation of the subsatellite region. 81

Fig. 7a. Infrared image of the underlying surface and of the clouds, obtained from Nimbus-1 on 15 September 1964 (Loop No. 271, 23 hrs 49 min, Moscow time). 82

Fig. 7b. Synoptic situation of the subsatellite region. 82

Fig. 8a. Infrared image of the clouds obtained from the Cosmos-122 on 22 September 1966 (Loop No. 1323, 15 hrs 03 min, Moscow time) 83

Fig. 8b. Synoptic situation of the subsatellite region. 83

Fig. 9a. Infrared image of the underlying surface and of the clouds, obtained from the Cosmos-122 on 4 July 1966 (Loop No. 135, 12 hrs 33 min, Moscow time). 84

Page

Fig. 9b. Measured field of radiation temperatures. 85

Fig. 9c. Synoptic situation of the subsatellite region. 85

Table 6. Comparison of measured and computed radiation temperatures 86

Table 7. Comparison of measured and computed magnitudes of the contrasts of radiation temperature. 86

Fig. 10a. Infrared image of the underlying surface and of the clouds, obtained from the Cosmos-122 on 9 July 1966 (Loop No. 209, 12 hrs 28 min, Moscow time). 87

Fig. 10b. Measured field of radiation temperatures. 87

Fig. 10c. Synoptic situation of the subsatellite region. 88

METHOD OF COMPUTING THE FIELD OF SHORT-WAVE RADIATION DURING ANISOTROPIC REFLECTION FROM THE UNDERLYING LAYER 90

Introduction 90

1. The Contribution which Reflection from the Underlying Surface Makes to the Brightness of Atmospheric Haze 90

Table 1. The contribution of the underlying surface to the brightness of haze at the upper limit of the atmosphere (values of the function $f(\tau_o A) = I_D^A/I_D$ for $\lambda = \kappa(\gamma) = 1$, $i = 30°$, $\theta = 0$ 91

Table 2. Contribution of the underlying surface to the brightness of haze at the upper limit of the atmosphere, with allowance for only a single scattering (values of the function $f_1(\tau_0, A) = I_{D_1}^A / I_{D_1})$, $\lambda = \kappa(\gamma) = 1$, $i = 30°$, $\theta = 0$ 92

2. Estimating the Absorption in the Atmosphere with the Respect to Single-Scattered Radiation 93

3. The Possibility of using a Lambert Scheme for Computed Scattered Radiation 94

4. The Effect of Anisotropy of Reflection on the Field of Scattered Radiation over a Water Surface 97

THE PROBABILITY OF OBSERVING CLOUDINESS AND THE UNDERLYING LAYER BY SIGNALS FROM AN INFRARED SYSTEM 100

Table 1. The probability of observing cloudiness against a background of various forms of radiating surfaces 102

Page

Table 2. The probability of observing various forms of radiating surfaces against the background of the basic noise of an infrared system 104

Fig. 1. The probability of observing dense stratocumulus clouds (1) and cumulus clouds (2), against the background of a continent, as a function of the level of the video signal 104

Fig. 2. Laws of distribution of video signals from dense stratocumulus and cumulus clouds with gaps, and from a dry-land surface. 105

Fig. 3. The probability of observing cumulus against the background of the ocean, as a function of the level of the video signal. 105

Fig. 4. The probability of observing a cyclone against the background of the ocean, as a function of the level of the video signal. 105

Fig. 5. Autocorrelation functions of video signals from a cyclone. 106

THE FIELD OF OUTGOING SHORT-WAVE RADIATION OVER THE OCEAN 108

1. Introduction 108

2. Reflection from a Rough Sea. Comparison with Specular and Anisotropic Reflection 109

3. A Scheme for Computing the Field of Short-Wave Radiation 112

Table 3. Integral field of outgoing short-wave radiation at the upper limit of the atmosphere over the ocean, $I_\pi(\theta, i, \phi)$ cal/cm$^2$-min-sterad. 113

4. The "Solar Path" on the Upper Limit of the Atmosphere. Comparison with a Lambert Sea 114

Table 5. Comparison with a Lambert Sea $f_i(\theta, \varphi) = \frac{I_\pi(\theta, i, \varphi)}{I'_\pi(\theta, i, \varphi)}$ 114

Fig. 1. Brightness of outgoing radiation (Zenith distance of the sun is 20°) $1 - I_\pi$, $2 - I'_\pi$. 115

Fig. 2. Brightness of outgoing radiation (Zenith distance of the sum is 80°). For symbols see Fig. 1. 115

Table 6. The contribution of scattered radiation to the field of outgoing short-wave radiation over the ocean $\frac{I_p}{I_\pi} = \frac{I''_0 + I_D}{I_\pi}$, v = 10 m/sec. 116

Page

THE CONTRIBUTION OF A DIFFUSE REFLECTION FROM A DEEP BODY OF WATER TO THE FIELD OF OUTGOING SHORT-WAVE RADIATION 117

Table 1. Radiation from the ocean $I(\theta)$ cal/cm$^2$-min-sterad 123

Table 2. Diffuse radiation from the ocean at the upper limit of the atmosphere $I'(\theta)$ cal/cm$^2$-min-sterad 123

Table 3. The field of outgoing short-wave radiation over the ocean, with allowance for scattering in the water layer, $I((\theta)_i, \phi)$ cal/cm$^2$ min-sterad 124

Table 4. The contribution of diffuse radiation from the ocean to the field of outgoing short-wave at the upper limit of the atmosphere $(I'(\theta))/(I(\theta,i,\phi))$ % cal/cm$^2$-min-sterad 125

RECONSTRUCTING A FIELD OF NEAR-GROUND PRESSURE FROM THE DATA OF WEATHER SATELLITES 127

Fig. 1. The actual field of near-ground pressure, 9 hrs, 14 February 1967. 130

Fig. 2. The reconstructed field of near-ground pressure, 9 hrs, 14 February 1967. 130

DETERMINING THE TEMPERATURE OF A RADIATING SURFACE AND THE TOTAL MOISTURE CONTENT ON THE BASIS OF RADIATION MEASUREMENTS MADE ON WEATHER SATELLITES 132

Fig. 1. Results from computing $T_0$ on the basis of data obtained from the Tyros-III weather satellite on 15 July 1961, orbit No. 44, Greenwich time 10 hrs 42 min - 10 hrs 55 min (on the right above and below are shown the values of $T_0$ as computed with the use of formulas (11') and (16), respectively). 137

Fig. 2. Results of computing $w_0$ g/cm$^2$ on the basis of data obtained from the Tyros-III weather satellite on 15 July 1961, orbit No. 44, 10 hrs 42 min - 10 hrs 55 min - Greenwich time. 138

Fig. 3. The results of computing $T_0$°C (plotted on the upper right) and $w_0$ g/cm$^2$ (lower right) on the basis of data obtained from the Cosmos-122 weather satellite, orbit Nos. 207 and 208, 9 hrs 15 min - 10 hrs 57 min, Greenwich time. 139

Fig. 4. Weather map for 12 hrs Greenwich time, 15 July 1961. 140

Page

Fig. 5. Weather map for 9 hrs, Moscow time, 9 July 1966. 141

THE EFFECT WHICH THE ANISOTROPY OF REFLECTION FROM THE UNDERLYING SURFACE HAS UPON THE DETERMINATION OF THE FLUX OF OUTGOING SHORT-WAVE RADIATION ON THE BASIS OF MEASUREMENTS MADE WITH WEATHER SATELLITES 142

Introduction 142

1. Deviation from a Lambert Field of Outgoing Short-Wave Radiation over Snow and over the Sea 143

Table 1. Mean values and dispersion of the relative deviation of the field of outgoing short-wave radiation from a field isotropic reflection for the ocean and for snow 144

2. The Effect of the Anisotropy of the Reflection on Outgoing Radiation for Various Values of Albedo 144

3. Applicability of the Lambert Scheme of Transformation 146

Table 2. The function $\phi(i, \theta)$ sterad$^{-1}$ (cal/cm$^2$-min)$^{-1}$ 147

Table 3. Regions of applicability of the Lambert scheme in the case of the ocean 147

Table 4. Permissible deviations from isotropic reflection for a snow surface $\Delta R' = (\Delta F/A)\Phi(i, \theta)$ [sterad$^{-1}$], $\Delta F = 0.04$ cal/cm-min 148

4. The Role of Clouds. Conclusion 148

DETERMINING WIND VELOCITY AND THE DEGREE OF WAVE ACTION ON THE BASIS OF MEASUREMENTS MADE FROM ARTIFICIAL SATELLITES OF THE BAROMETERS OF THE "SOLAR PATH" 150

1. Introduction 150

2. Sensitivity of the Field of Brightness of Outgoing Short-Wave Radiation to Wind and to Wave Actions 150

Table 1. Spectral field of outgoing radiation over the ocean at the upper limit of the atmosphere, for various wind velocities $I_v(\lambda, i, \theta, \phi)$ [μcal/cm$^2$-min-sterad] 152

Table 2. The contribution of scattered radiation to the field of outgoing radiation at the upper limit of the atmosphere $\left(\frac{I_\sigma(\lambda, i, \theta, \varphi)}{I_p(\lambda, i, \theta, \varphi)}\right)$ 153

Page

Table 3. Transverse gradient of the "solar path" at the upper limit of the atmosphere μcal/cm$^2$-min-sterad-deg 154

Table 5. Relative values of the maximum of the "solar path" at the upper limit of the atmosphere, for various wind velocities 155

3. Difficulties and Prospects of the Method 155

THE PROBLEM OF AVERAGING IN MEASURING HYDROMETEROLOGICAL FIELDS 158

Fig. 1. The normed (that is, divided by the doubled dispersion) square of the mean-square deviation of the true value of the hydrometeorological element at point r from its value averaged within the limits of interval θ.

1) $\alpha = 0.1$ km$^{-1}$; $\theta = 1$ km; 2) $\alpha = 0.1$ km$^{-1}$, $\theta = 0$; 3) $\alpha = 0.1$ km$^{-1}$, $\theta = 5$ km; 4) $\alpha = 0.1$ km$^{-1}$, $\theta = 10$ km 160

Fig. 2. The normed correlation function k (r) and the polynormed (that is, divided by the doubled dispersion) structural function B (r, θ) of the values of the hydrometeorological element averaged over the interval θ.

1) $\alpha = 0.5$ km$^{-1}$, $\theta = 1$ km; 2) $\alpha = 1$ km$^{-1}$, $\theta = 1$ km; 3) $\alpha = 0.1$ km$^{-1}$, $\theta = 0$; 4) $\alpha = 0.1$ km$^{-1}$, $\theta = 1$ km; 5) $\alpha = 0.1$ km$^{-1}$, $\theta = 10$ km; 6) $\alpha = 0.5$ km$^{-1}$, $\theta = 10$ km; 7) $\alpha = 1$ km$^{-1}$, $\theta = 10$ km; 8) $\alpha = 0.1$ km$^{-1}$; 9) $\alpha = 0.5$ km$^{-1}$; 10) $\alpha = 1$ km$^{-1}$. 162

Fig. 3. The normed structural function of the values of hydrometeorological element averaged within the limits of the interval θ.

1) $\alpha = 0.5$ km$^{-1}$, $\theta = 0$; 2) $\alpha = 0.5$ km$^{-1}$, $\theta = 1$ km; 3) $\alpha = 0.5$ km$^{-1}$, $\theta = 5$ km; 4) $\alpha = 0.5$ km$^{-1}$, $\theta = 10$ km; 5) $\alpha = 0.5$ km$^{-1}$, $\theta = 0$; 6) $\alpha = 0.1$ km$^{-1}$, $\theta = 1$ km; 7) $\alpha = 0.1$ km$^{-1}$, $\theta = 5$ km; 8) $\alpha = 0.1$ km$^{-1}$, $\theta = 10$ km. 163

Fig. 4. The normed space correlation function k(r) and the polynormed (that is, divided by the doubled dispersion) structural function B(r, θ) of the temperature of water surface averaged over the interval θ, in the region of the Gulf Stream.

$m(x) = 20.2°C$, $D = 0.531$ deg$^2$, $\sigma = 0.728$ deg

1) $\theta = 0$; 2) $\theta = 1$ km; 3) $\theta = 5$ km; 4) $\theta = 10$ km; 5) $k(r) = e^{-0.325r}$ cos 0.418 r miles; 6) $k(r) = e^{-0.175r}$ cos 0.225 r km 164

CERTAIN PATTERNS IN THE VERTICAL DISTRIBUTION OF OUTGOING LONG-WAVE RADIATION 167

Table 1. The connection between $u_z$ and $\sigma T_o^4$. 169

Page

Table 2. Relationships between (a) outgoing long-wave flux $u_z$ and the ratio $u_z/\sigma T_o^4$, and (b) air temperature $t_z$, effective water-vapor content $w_z$, and the ground-air temperature gradient $\Delta t = t_o - t_z$. 169

Fig. 1. The dependence of the flux of outgoing long-wave radiation $u_z$ upon temperatue (a) and upon water vapor content (b)
1, 4 November; 2, 2 October; 3, 12 August. 170

Fig. 2. The dependence of the ratio $u_z/\sigma T_o^4$ upon the ground-air temperature gradient (a), and upon the water vapor content in the atmospheric layer for which $\Delta t$ = const (b), at Minsk station.
1, $\Delta t = 10.0°$; 2, $\Delta t = 20.0°$; 3, $\Delta t = 40°$. 171

Fig. 3. Vertical profiles of outgoing long-wave radiation and air temperature, on 27 August (1) and 6 November (2). 172

Table 3. Relationship between $u_z/\sigma T_o^4$ and $\Delta t$. 172

Table 4. Mean values of the ratio $u_z/u_o$. 173

Table 5. Initial data used in the calculation 175

Fig. 4. Dependence of $u_z^{(2)}/\sigma T_o^4$ (a) and $u_z^2/\sigma T_{o,z}^4$ (b) upon water-vapor content. 176

Table 6. Outgoing flux $u_z$ and its components $u_z^{(1)}$ and $u_z^{(2)}$ at various levels in the troposphere 177

Fig. 5. The connection between the relative variation in outgoing long-wave flux and the ground-air temperature gradient. 179

Table 8. Comparison of outgoing long wave flux, computed with allowance for water vapor ($H_2O$), and with allowance for both water vapor and carbon dioxide ($H_2O + CO_2$)

$$\Delta u_z = u_{z\,H_2O + CO_2} - u_{z\,H_2O}$$ 181

Table 9. Recurrence (in%) of the ratio $u_z^\phi/u_z$ at various altitudes (data from 6 points). $u_z^\phi$ is outgoing long-wave flux as computed by formula; $u_z$ is the flux as measured by radiosonde. 182

Table 10. Recurrence of $u_z^d/u_z$ at various altitudes (data from 6 points). 182

Page

Fig. 6. Comparison of vertical profiles of the flux of outgoing long-wave radiation.
1, computed by the Shekhter diagram; 2, by formula (2);
3, measured 184

THE SPECTRAL BRIGHTNESS OF CLOUDS AND OBJECTS ON THE LANDSCAPE WITHIN THE VISIBLE AND THE NEAR INFRARED PORTIONS OF THE SPECTRUM 185

1. Apparatus and Method of Measurement 185

2. Results of the Measurements 187

Table 3. Mean brightness of clouds and terrestrial objects in Mw/cm$^2$-sterad, recorded during the period May to June 1966, on the European territory of the Soviet Union, for various spectral intervals and for various altitudes of the sun 188

Fig. 1. A mean spectral brightness of objects for various altitudes of the sun: 1, Cirrus clouds, $H_\odot = 40°$; 2, cumulus clouds, $H_\odot = 30°$; 3, old ice with snow, $H_\odot = 26\text{-}29°$; 4, multi-level cloudiness, $H_\odot = 36\text{-}42°$; 5, deserts and semi-deserts, $H_\odot = 34\text{-}36°$; 6, tundras containing patches (10-20%) of snow, $H_\odot = 43\text{-}46°$. 189

Fig. 2. Mean spectral brightnesses of clouds at the middle level for various altitudes of the sun.
1, $H_\odot = 42\text{-}55°$; 2, $H_\odot = 32\text{-}42°$; 3, $H_\odot = 21.7 - 32.0°$; 4, $H_\odot = 12.5\text{-}21.7°$; 5, $H_\odot = 1\text{-}2°$. 190

Fig. 3. Mean and extreme values, and recurrence (%) of various gradiations of the spectral brightness of cloudiness at the middle layer, for altitudes of the sun of 42-45°. 191

Fig. 4. Mean and extreme values and recurrence (%) of various gradations of spectral brightness of a thick layer of cumulus clouds at altitudes of the sun from 42-45°. 192

3. Comparison of Experimental Data with the Results of Theoretical Calculations 192

Table 4. Comparison of the measured and the computed values of absolute spectral brightness of cloudiness B mw/cm$^2$-sterad μm (means values are given in the first line , the maximum values in the second line) 193

4. Comparison of the Results of Spectrometric and Pyranometric Measurements 194

Page

Fig. 5. Comparison of the fluxes of solar radiation reflected by clouds, as measured with the pyranometer $E_p^{\uparrow}$ and the spectrometer $E_s^{\uparrow}$. 195

THE EXPERIMENTAL STUDY OF THE SCATTERING OF LIGHT BY CLOUD PARTICLES. I. THE MODELING OF WATER DROPLETS 198

Fig. 1. Curves of the spectral transmission of two types of glass, STF1(1) and TF6 (2). 200

Fig. 2. Dispersion curves for water (1), model I (2) and model II (3). 201

Fig. 3. The design of a device for producing glass spheres. 201

THE EXPERIMENTAL STUDY OF THE SCATTERING OF LIGHT BY CLOUD PARTICLES. II. THE MEASUREMENT OF THE INDICATRIXES OF THE SCATTERING OF LIGHT OF MODELS OF WATER DROPLETS 205

Fig.1. Design of the measuring apparatus.
1, photoelectric cell; 2, amplifier; 3, EPPV-60; 4, beam; 5, motor; 6, photomultiplier; 7, objective lens; 8, neutral light filters; 9, light trap; 10, disc; 11, motor; 12, transmission gear case; 13, worm; 14, worm wheel; 15, absolute blackbody; 16, polaroid; 17, light filter; 18, objective lens. 206

Fig. 2. Electrical measuring circuit of the apparatus.
1, photoelectric cell; 2, mercury vapor lamp; 3, cuvette; 4, photomultiplier; 5, motor; 6, amplifier. 207

CERTAIN CHARACTERISTICS OF THE STRUCTURE OF THE INTENSITY FIELD OF CLOUDS WHICH APPEAR IN STEPPE AREAS AND IN SEMI-DESERT AREAS 212

Table 1. Recurrence (%) of rain of various maximal intensity. 213

Table 2. Recurrence (%) of precipitation of various intensity (shown in the enumerator), and the proportion of precipitation of given intensity among the total (shown in the denominator) 214

Table 3. Incremental proportion (%) of precipitation of various intensity with respect to total duration (1) and with respect to total precipitation (2) 214